Dragana Mihajlović[1*], *Bojan Medjo*[1], *Jelena Bajat*[1], *Veljko Djokić*[1,2]

DAMAGE BEHAVIOUR OF COMMERCIALLY PURE TITANIUM IN THE HUMAN BODY

PONAŠANJE OŠTEĆENJA KOMERCIJALNOG ČISTOG TITANIJUMA U LJUDSKOM TELU

Originalni naučni rad / Original scientific paper
Rad primljen / Paper received: 10.02.2026
https://doi.org/10.69644/ivk-2026-01-0038

Adresa autora / Author's address:
[1)] University of Belgrade, Faculty of Technology and Metallurgy, Belgrade, Serbia

D. Mihajlović https://orcid.org/0000-0003-3966-1909 ;
B. Medjo https://orcid.org/0000-0001-8100-7519 ;
J. Bajat https://orcid.org/0000-0003-0742-8176 ;
V. Djokić https://orcid.org/0000-0003-2541-0420
[*]email: dbarjaktarevic@tmf.bg.ac.rs
[2)] Innovation Centre of the Faculty of Technology and Metallurgy, Belgrade, Serbia

Keywords
- anodic oxidation
- corrosion resistance
- high pressure torsion
- ultrafine-grained titanium
- scratch test

Abstract

In order to optimise surface characteristics, corrosion and scratch damage, as important factors for accepting a metallic implant at conditions of a human body, commercially pure titanium (cpTi) can be modified by different treatments, including high pressure torsion (HPT) and anodic oxidation (AO). Here, a nanotube oxide layer on the surface of ultrafine-grained commercially pure titanium (UFG cpTi) is formed using AO in 1M H_3PO_4 + NaF solution during 60 min. SEM microphotographs show that AO with selected parameters can lead to the formation of a highly regular oxide layer with nanotubes on the surface of UFG cpTi. Determination of the surface contact angle shows that the surface of UFG cpTi after AO is more hydrophilic than before AO treatment. In order to characterise the surface topography and adhesion of formed nanotubes, scratch testing on the UFG cpTi surface after AO treatment is done. Corrosion resistance is tested in Ringer's solution with pH value of 5.5 at 37 °C to simulate the environment in the human body. UFG cpTi before and after AO is analysed by electrochemical impedance spectroscopy (EIS) and potentiodynamic polarisation. The inner barrier and outer porous surface layers are highly resistant with capacitive behaviour for both tested materials, but the synergistic action of HPT and AO treatments led to improved corrosion resistance and therefore a reduced corrosion rate for commercially pure titanium in the conditions of the human body.

Ključne reči
- anodna oksidacija
- koroziona otpornost
- uvijanje pod visokim pritiskom
- sitnozrni titan
- test grebanjem

Izvod

U cilju optimizacije površinskih karakteristika, otpornosti prema koroziji i oštećenja usled grebanja, koji predstavljaju ključne faktore za prihvatanje metalnih implantata u uslovima ljudskog organizma, komercijalno čisti titanijum (cpTi) može se modifikovati različitim postupcima, uključujući uvijanjem pod visokim pritiskom (HPT) i anodnom oksidacijom (AO). Nanocevni oksidni sloj je formiran na površini sitnozrnog komercijalno čistog titana (UFG cpTi) primenom AO u rastvoru 1 M H_3PO_4 + NaF tokom 60 min. SEM snimci pokazuju da primena AO pri odabranim parametrima dovodi do formiranja visoko organizovanog nanotubularnog oksidnog sloja na površini UFG cpTi. Merenja kontaktnog ugla pokazuju da površina UFG cpTi nakon AO postupka ima veću hidrofilnost u poređenju sa površinom pre tretmana. Radi karakterizacije topografije površine i adhezije formiranih nanocevi, sprovedena su ispitivanja grebanjem (scratch test) na uzorcima UFG cpTi pre i posle AO tretmana. Otpornost prema koroziji ispitivana je u Ringerovom rastvoru pri pH = 5,5 na temperaturi 37 °C, kako bi se simulirali uslovi u ljudskom organizmu. Uzorci UFG cpTi, pre i nakon AO, su analizirani metodama elektrohemijske impedanse spektroskopije (EIS) i potenciodinamičke polarizacije. Unutrašnji barijerni i spoljašnji porozni slojevi pokazuju visoku otpornost i kapacitivno ponašanje kod oba ispitivana materijala, dok zajedničko dejstvo HPT i AO tretmana dovodi do poboljšane otpornosti na koroziju i smanjenja brzine korozije komercijalno čistog titana u uslovima ljudskog organizma.

INTRODUCTION

Titanium-based materials have a combination of several great properties: good mechanical and chemical properties, low density (4.5 g/cm^3), corrosion resistance and biocompatibility which are the main reasons for using it in the manufacture of medical implants. Commercially pure titanium (cpTi) and titanium alloys are the most used metallic materials for implant fabrication, such as wires and screws for bone fixation, dental implants, orthopaedic wires and prostheses, and cardiovascular stents /1/ where Ti-6Al-4V is the most present titanium based material, with a share of up to 45 % in total implant fabrication, /2/. There are four grades of cpTi used in implant manufacture that differ in impurity content. Oxygen, iron and nitrogen in the chemical composition of cpTi have to be precisely controlled, with the amount of oxygen having a particularly large influence on the elasticity and tensile strength of cpTi, /3/. cpTi is nontoxic and is inert in the human body which makes it ideal for bio-implants, though its biological role in the human body is not entirely clear, /2/. However, effects like allergic reactions have been observed in titanium based bio-implants, often due to the release of Al and V alloying elements /2/. Today,

development of a new generation of β-titanium alloys leads to the use of alloying elements such as: Mo, Ta, Nb, and Zr. Table 1 presents a comparison of titanium-based bio-implant materials. Disadvantages of this group of metallic biomaterials are the possibility of corrosion damage in the presence of body fluids which can cause a problem during contact of the implant with surrounding tissues, and increased wear due to external loads during implant-bone contact, /4, 5/. As a consequence of the direct contact of metallic biomaterial with body fluid, metallic ions are released into surrounding tissues which can cause local, but also serious, systemic health problems due to the diffusion of ions throughout the body; this is a general problem with practically all metallic biomaterials. The degree of corrosion resistance depends on the microstructure of the implant material, the presence of unevenness on the surface /6/, composition, temperature and pH value of the environment. It has been proven that the decrease in pH value of the environment leads to an increase in the concentration of released ions from the metallic implant /7, 8/. Interstitial fluids in the human body contain water, dissolved oxygen, proteins and various ions, so they represent a very aggressive environment for metallic implant materials which is why corrosion resistance of metallic biomaterials is a very important segment, both for aesthetic appearance, strength and biocompatibility /3, 9, 10/. As a result of the corrosion process, the surface oxide layer is damaged, and metallic ions are released into surrounding tissues. It is known that implants will typically not fail during their use due to fracture directly caused by corrosion, but the occurrence of fracture is possible as a consequence of the combined effect of wear or fatigue and corrosion. For example, implant fatigue leads to the formation of cracks in the oxide layer of biomaterial surface which are subject to corrosion /11, 12/. Besides, the dissolution of metallic biomaterials, due to corrosion, can lead to erosion and eventually to implant failure /11, 12/. Typical failure of orthopaedic implants as a result of fatigue occurs due to a reduction in strength and due to the formation of corrosion pits. Also, dental implants are susceptible to corrosion damage in the extremely aggressive environment of the oral cavity. When implanting metallic material into the human body, a major problem is the electrolytic effect of the environment. Titanium and its alloys generally exhibit good corrosion resistance due to the presence of a stable TiO_2 passive layer; however, exposure to Ringer's solution which simulates physiological body fluids, can still lead to surface degradation. The chloride ions present in Ringer's solution may disrupt the protective oxide film, initiating localised corrosion such as pitting and crevice attacks. Furthermore, under cyclic loading or micromotion conditions, tribocorrosion may occur, combining mechanical wear with chemical dissolution. This degradation not only weakens the material surface but can also lead to the release of titanium ions and particles into the surrounding environment, potentially affecting biocompatibility and long-term implant stability, /13/. Titanium alloys with niobium (Nb) and zirconium (Zr), as alloying elements, show very good corrosion resistance in biologically simulated conditions, such as Ringer's solution. For example, the Ti-13Zr-13Nb alloy prepared by the direct electrochemical reduction method shows a lower corrosion current density (j_{corr}) compared to cpTi after 10 days of immersion in Ringer's solution, indicating a more stable passive layer /14/. Also, the pH of the solution and the presence of fluorine ions significantly affect the corrosion behaviour of Ti-Nb-Zr alloys. The study examines Ti-5Nb-13Zr, Ti-13Nb-13Zr and Ti-20Nb-13Zr alloys in Ringer's solution at different pH values and with/without 1000 ppm fluorine. Results show that the lower the pH value and the addition of fluorine increase corrosion, while Ti-13Nb-13Zr is generally more resistant than the other variants and in most conditions has a higher resistance than cpTi, /15/. Also, for titanium alloys that have other elements in addition to Nb and Zr, e.g., Ti-23.6Nb-5.1Mo-6.7Zr alloy, experimental results in Ringer's solution show that after certain thermomechanical treatments the alloy forms a passive layer with high protection, and the corrosion current is very low (~ nA/cm^2) which indicates an extremely stable oxide film, /16/.

Table 1. Comparison of titanium-based bio-implant materials, /4/.

Materials	Composition	Advantages	Disadvantages
cpTi (Grades 1-4)	Pure titanium	Excellent biocompatibility, corrosion resistance, well-established clinical success	Lower strength; higher elastic modulus can lead to stress shielding; potential for allergic reactions in some patients
Ti-6Al-4V (Grade 5)	90 % Ti, 6 % Al, 4 % V	High strength and fatigue resistance; widely used in biomedical applications	Potential for ion release (Al, V); may cause adverse reactions in sensitive individuals
Ti-Zr-Nb-Ta alloys	Ti with varying Zr, Ta, Nb content	Enhanced strength and corrosion resistance; reduced ion release compared to Ti-6Al-4V	Limited clinical data; potential for higher stiffness leading to stress shielding

One of the directions of further development of titanium-based materials is the application of various modern procedures of severe plastic deformation (SPD). The main goal of the SPD is to obtain ultrafine-grained (UFG) metallic materials /17-21/ with enhanced mechanical strength and surface reactivity. HPT processing refines the grain size of cpTi down to the submicrometer or nanometre scale, increasing the density of grain boundaries and potentially altering corrosion and wear behaviour. One of the basic expectations is that decreasing the grain size should lead to improvement of corrosion resistance, because the increased grain boundary density can promote faster formation and regeneration of protective oxide film (TiO_2) that protects the surface from further electrolyte attack, /22/. Several studies confirm this hypothesis, stating that UFG cpTi shows lower corrosion currents (j_{corr}) and more favourable passivation potentials in physiological solutions such as Ringer's or Hank's /23/. For example, Zhang et al. /24/ show that UFG cpTi forms a more compact, stable, and homogeneous oxide layer, while Miyamato et al. /25/ report that corrosion rate of UFG cpTi is reduced compared to CG cpTi. On the other hand, a significant number of studies indicate deterioration of corrosion resistance after HPT treatment. Ultrafine-grained (UFG) Ti often shows improved corrosion resistance because the high

grain-boundary density accelerates passive-film formation and yields a more uniform TiO_2 layer, resulting in lower j_{corr} and more positive corrosion potentials compared with coarse-grained Ti, /26/. Some studies point out that high degree of deformation stresses, internal defects and residual stresses that remain after HPT, can destabilise the passive layer and promote localised corrosion, especially in solutions with chloride ions /12/. For example, Yu et al. /27/ show that UFG Ti-6Al-7Nb has higher corrosion current density and lower passivation potentials in Ringer's solution compared to conventional samples; it is typically attributed to oxide film instability and heterogeneous voltage field. Some studies point out that differences in results arise from different parameters of HPT processing, such as pressure, number of revolutions, temperature, as well as from different post-deformation treatments (e.g., annealing, polishing, anodising).

Also, chemical composition and phase play a significant role, e.g., β-stabilised alloys (Ti-Nb, Ti-Nb-Zr, Ti-Nb-Ta) often show different reactions to HPT than α or α+β alloys. In addition to SPD processes, to enhance biocompatibility, corrosion resistance, and surface mechanical performance, metallic biomaterials commonly undergo surface modification procedures, /19/. Among these techniques, anodic oxidation (AO) is widely used to produce controlled nanotubular or nanoporous oxide layers, ideally with minimal or no interchannel spacing. Such engineered TiO_2 surface morphologies are expected to improve corrosion resistance /28, 29/, biocompatibility, and wear behaviour. AO further modifies the surface by creating a porous oxide layer-usually composed of TiO_2 in anatase and rutile forms - that increases the corrosion resistance and promotes osseointegration. The oxide morphology can be tailored (e.g., nanotubular, nanoporous) to enhance cell adhesion and limit ion release. However, under long-term physiological loading, the oxide layer may still suffer from cracking, delamination, or local dissolution, especially in aggressive biological environments containing proteins or fluorides. The synergistic use of HPT and anodisation has shown promising results, as the dense UFG substrate supports the adherence of the anodic oxide, while the surface layer provides a strong barrier against corrosion and wear. Nonetheless, discrepancies exist among studies, as processing parameters (pressure, number of HPT turns, voltage and duration of anodisation) greatly influence the microstructural homogeneity and long-term stability of the implant. Overall, degradation of cpTi in the human body is a multifactorial process involving mechanical, electrochemical, and biological effects. The main objective of this study is to focus on improving the long-term stability of cpTi by optimising microstructure, surface treatments, and protective coatings. The specific objective is to examine the influence of the AO process on the resistance of UFG cpTi in Ringer's solution, through corrosion behaviour examination. The results should allow a better understanding of the corrosion behaviour of UFG cpTi after the AO in the aggressive conditions of the human body.

MATERIALS AND METHODS

Materials preparation

- High-pressure torsion

In order to obtain an UFG structure, CG cpTi (grade 2) is subjected to severe plastic deformation using the HPT procedure. The HPT procedure is performed at a temperature of 24±1 °C under a pressure of 4.1 GPa and a speed of 0.2 rpm with 5 rotations. Chemical composition of commercially pure titanium is presented in Table 2. The appearance of titanium samples before and after HPT processing the and schematisation of experimental set-up of the HPT process are presented in Fig. 1a.

Table 2. Chemical composition of commercially pure titanium.

Elements	Ti	O	H	N	C	F
[mas. %]	99.3	0.25	0.015	0.03	0.10	0.30

- Anodic oxidation

After HPT procedure, the AO is performed using a system of two electrodes: platinum as cathode, and a sample of UFG cpTi as the working electrode, or anode. AO is performed

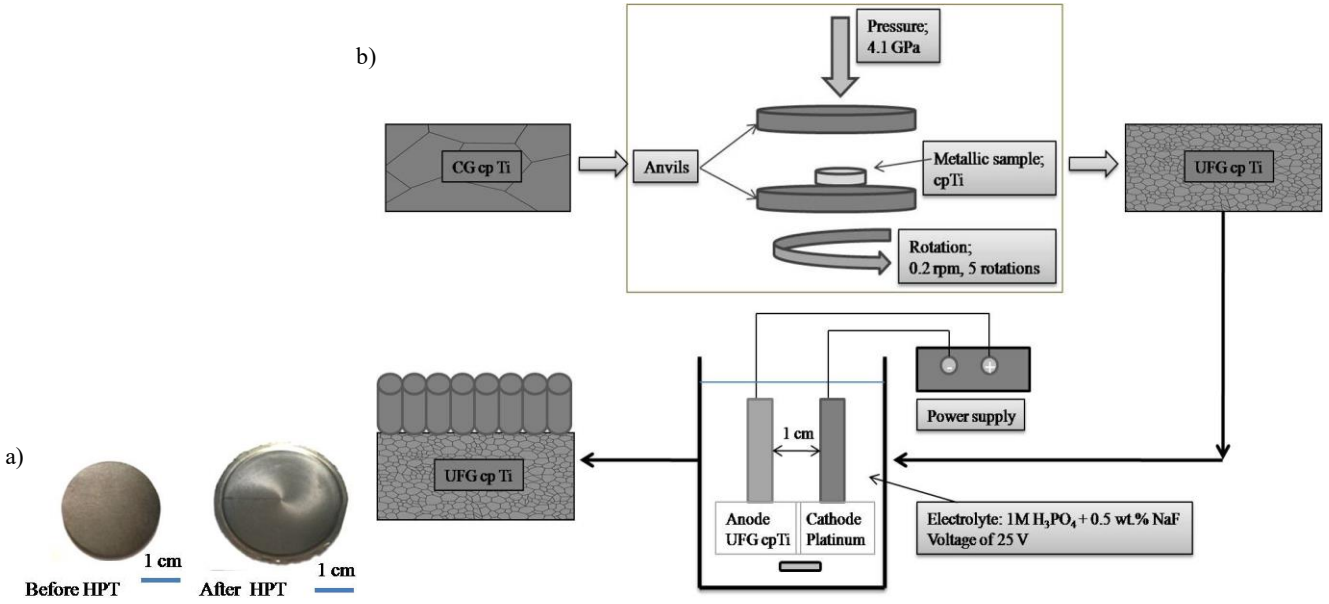

Figure 1. a) Titanium samples before and after HPT processing; and b) schematization of experimental set-up of HPT and AO process /1, 41/.

at room temperature, at a voltage of 25 V. 1 M H_3PO_4 + 0.5 wt.% NaF is chosen as the electrolyte, while the duration of anodic oxidation is 60 min. Schematisation of experimental set-up of the AO process is presented in Fig. 1b.

Scratch test

A testing machine Nanoindenter G200 with Berkovich-type diamond tip indenter is used to perform the test by making scratches. Scratch length was 700 μm (with 50 μm/s) and the load progressively raised to 40 mN, Fig. 2. The scratch test is performed under a controlled and progressively increasing normal force. It involves three steps: (i) applying a low load to assess the surface morphology; (ii) increasing the normal force along the same scratch path up to maximum load; and (iii) applying a small load to evaluate residual surface deformations.

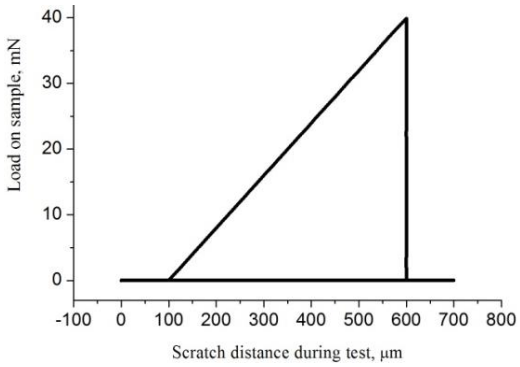

Figure 2. Load on the samples during scratch testing, /30/.

- Corrosion behaviour examination

Corrosion resistance of UFG cpTi before and after AO is tested by two methods: the potentiodynamic method and the electrochemical impedance spectroscopy (EIS) using Gamry Reference 600 potentiostat/galvanostat/ZRA device. Tests are performed in a Ringer's solution (Hemofarm, Serbia), with pH = 5.5 at 37 °C in order to simulate the environment in the human body. Chemical composition of Ringer's solution is presented in Table 3.

Table 3. Chemical composition of Ringer's solution.

Chemical composition	NaCl	KCl	$CaCl_2 \cdot 2H_2O$
[g/L]	8.60	0.30	0.33

The system for testing corrosion resistance consists of three electrodes. The working electrode is the tested material sample, the counter electrode is platinum wire, while the reference electrode is a saturated calomel electrode (SCE) in the form of a probe. With Gamry Instruments Framework software package, the potential change in the open circuit (E_{oc}) is monitored over a period of 30 min, and after establishing a stationary state, measurements are made using the potentiodynamic method in the potential range -1.0 to 4.0 V. Anode and cathode polarisation curves are recorded at a potential change rate of 1.0 mVs^{-1}. The analysis of impedance values is presented in Nyquist and Bode planes. A model of a two-layer oxide, consisting of inner barrier layer and an extern porous layer is used. The corresponding equivalent circuit (EC) is used to fit the results.

RESULTS AND DISCUSSION

Anodising UFG cpTi for different time

Figure 3a shows the modified UFG cpTi surface after AO for 60 min. As can be seen from the SEM micrograph, the AO that lasted 60 min. led to the formation of nanotubes as part of the oxide layer. Figure 3b presents the current density during the AO process of UFG cpTi for 60 min. Several studies have reported that increased current density promotes the formation of a more uniformly distributed and thicker layer of nanotubes, /31, 32/.

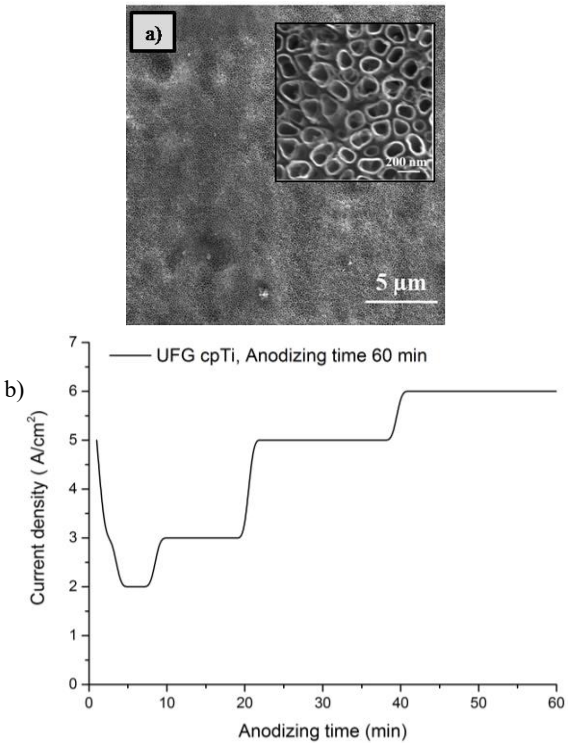

Figure 3. a) SEM micrograph of modified UFG cpTi surface after AO for 60 min; b) current density during AO of UFG cpTi, for 60 min.

After AO of UFG cpTi for 60 min, the formed nanotubes have average diameter of 100 nm and average wall thickness of 30 nm. The standard deviation (SD) of 30 measurements for mean values of nanotube sizes is: 8.60 nm nanotube diameter; and 0.69 nm nanotube wall thickness. Measurements of nanotube sizes are done using Image J software.

Also, AO is also done for 30, 90 and 120 min, but the homogeneous nanotube structure is not obtained as an integral part of the modified oxide layer on the surface of UFG cpTi. These samples are excluded from further testing, but a brief overview of their surface morphology is given here. The modified structure of UFG cpTi after AO for 30, 90, and 120 min. is presented in Figure 4. After AO for 30 min, Fig. 4a, the surface shows irregular pore openings with visible areas where nanotubes are not yet fully formed. Nanotube contours are shallow and not sharply defined, indicating early-stage oxide dissolution-formation competition. Short anodisation time does not allow for complete dissolution of the initial compact oxide and full development of vertically aligned nanotubes. The UFG structure may accelerate oxide growth at the beginning, but 30 min is insufficient for stable

tube elongation. After AO for 60 min, nanotube structure is significantly more homogeneous and continuous compared to 30 min. Nanotube openings appear uniform, circular/elliptical, and densely packed. The nanotube layer is well organised, with clearer boundaries and more regular spacing. The zoomed SEM image shows consistent tube diameters and smooth walls, a characteristic of optimised growth conditions, Fig 4a. After AO for 60 min, anodisation reaches a balance between oxide formation and dissolution, leading to stable, well-ordered nanotubes. This time appears close to optimal for achieving high morphological regularity on UFG cpTi.

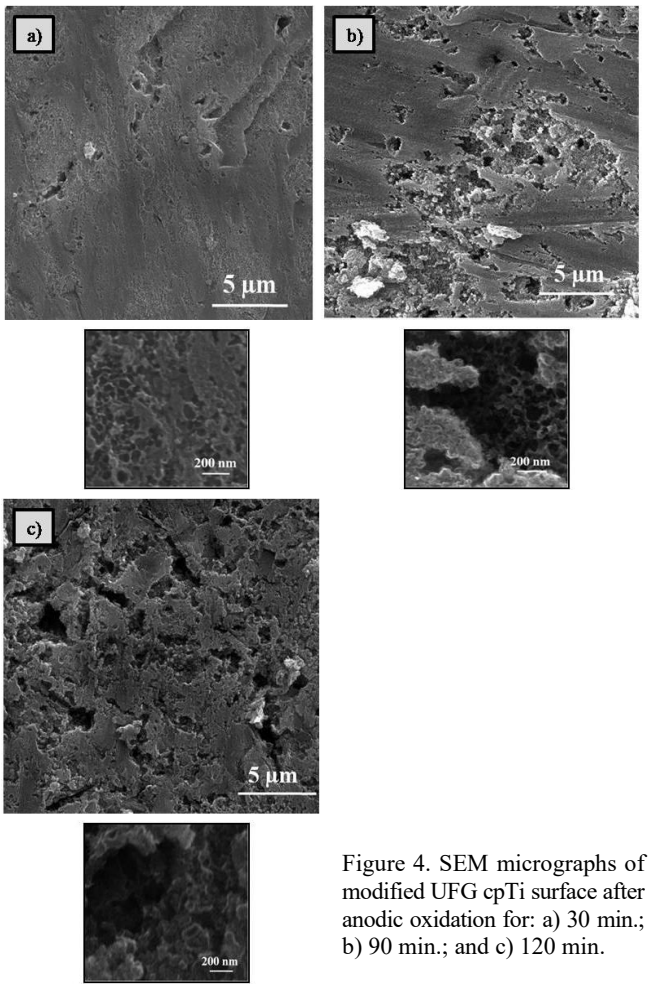

Figure 4. SEM micrographs of modified UFG cpTi surface after anodic oxidation for: a) 30 min.; b) 90 min.; and c) 120 min.

After AO for 90 min, Fig. 4b, the surface shows partial roughening and fragmentation of nanotube layer. Some regions exhibit agglomerated oxide debris, possibly due to over-dissolution or local delamination. Nanotube openings become less regular, and the structure appears less compact than after 60 min. Nanotube walls look thicker and more irregular, indicating the onset of structural destabilisation. After AO for 120 min, Fig. 4c, the nanotube layer is highly porous, disordered, and heavily fragmented. Nanotube openings are irregular, large, and poorly defined, suggesting advanced over-etching. The layer appears partially collapsed, with some areas transitioning into a sponge-like oxide, rather than discrete tubes. The SEM image, Fig. 4c, confirms severe structural degradation, with no clear tube organisation remaining. Figures 4a and 4b show that anodisation of UFG cpTi leads to the formation of self-organised TiO_2 nanotube layers, but their morphology strongly depends on anodisation duration. As time increases, several characteristic features evolve: (i) degree of ordering; (ii) tube opening and wall definition; (iii) surface integrity; and (iv) presence of degradation phenomena such as tube collapse or layer delamination. Excessively long anodisation causes nanotubes to lose mechanical stability. Continuous chemical dissolution leads to wall thinning, tube merging, and eventual breakdown of the ordered nanotube array /33-35/. These results clearly demonstrate that anodisation time is a key parameter determining the quality of TiO_2 nanotubes grown on ultrafine-grained Ti. The UFG substrate generally promotes faster oxide growth due to enhanced diffusion along grain boundaries, meaning the optimal anodisation time may be shorter than for conventional coarse-grained titanium /35-37/. More about the surface morphology of titanium-based materials after modification by AO can be found in our previous papers /38-40/. Table 4 presents the chemical composition of nanostructured oxide layer obtained after AO of UFG cpTi, for 60 min.

Table 4. Mean values of chemical composition of nanostructured modified surface of UFG cpTi after AO for 60 min.

Material	Anodising time (min)	Detected elements on sample surface (wt. %)			
		Ti	O	Na	P
UFG cpTi	60	57.05	42.74	0.34	0.26

The obtained results indicate the presence of Ti and O at 57.05 % and 42.74 %, in respect. One of the five analysed positions show the presence of Na and P at 0.34 % and 0.26 %, in respect. Presence of Na and P on the modified surface is a consequence of the residual electrolyte used during the electrochemical anodisation process.

Determination of surface contact angle of UFG cpTi after AO for 60 min

Photographs of the contact angle of UFG cpTi before and after AO are shown in Fig. 5, while values of contact angle are given in Table 5.

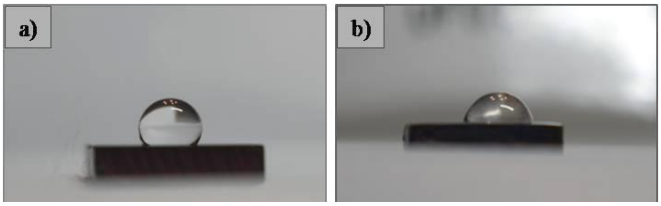

Figure 5. Contact angle images: a) UFG cpTi; b) UFG cpTi after AO.

Table 5. Contact angle for UFG cpTi before and after AO.

Material	UFG cpTi	UFG cpTi, AO, 60 min.
Contact angle [°]	126.1 ± 4.8	72.9 ± 4.7

The contact angle decreases after AO of UFG cpTi, making the surfaces of UFG cpTi more hydrophilic. In our previous paper, it is shown that roughness increases after AO of UFG cpTi /41/. These results show that increased roughness of the surface after AO, at the same time, leads to the decreased value of contact angle. Increasing roughness of UFG cpTi surface leads to increasing the surface region that the surrounding solution and tissue can contact, in other words it increases surface wettability. Previous studies have

demonstrated that the hydrophilicity of the metallic implant surfaces plays a crucial role in governing the adsorption of proteins, macromolecules, and bacteria, as well as in modulating the interactions of hard and soft tissues with the implant. Consequently, surface wettability has been directly linked to the extent of osseointegration observed at *in vivo* experiments, /42/.

Scratch resistance test of UFG cpTi after AO for 60 min.

Figure 6 presents a typical profile along the cross section of the scratched surface of UFG cpTi before and after AO. The cross section is composed of two regions: groove area (GA) and pile-up areas (PA_1, PA_2) (in Fig. 6 as black and gray, respectively).

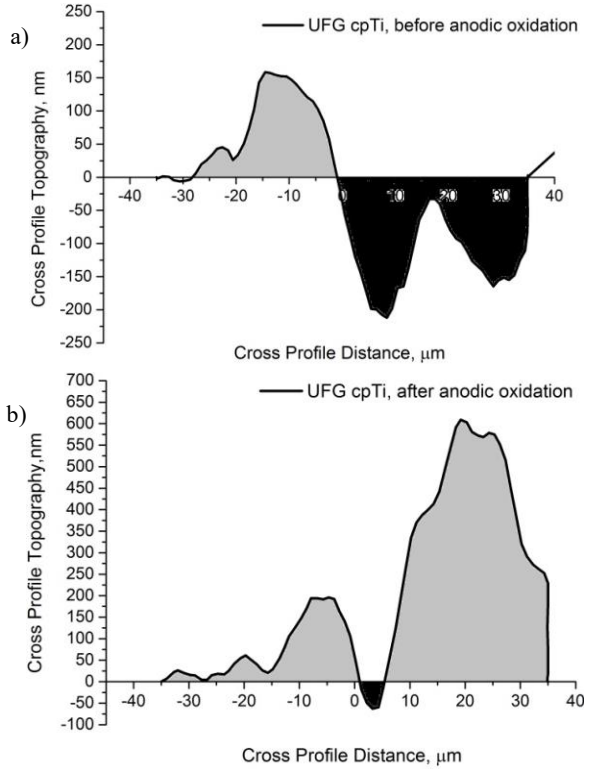

Figure 6. Profile of scratch cross section of the UFG cpTi surface: a) before and; b) after AO for 60 min.

Many previous studies define parameters PA and GA to characterise mechanisms of scratch testing metallic materials and their modified surface and define the criterion for the method of removing material as 'ploughing' dominant or 'shearing' dominant mechanism, /43/. If $PA_1 + PA_2 = GA = 0$, the dominant mechanism of the scratch test is rubbing, and if $PA_1 + PA_2 = GA \neq 0$, the dominant mechanism of the scratch test is elastic-plastic transition. On the other hand, if $PA_1 + PA_2 > GA$, the dominant mechanism of the scratch test is ploughing, and if $PA_1 + PA_2 < GA$, the dominant mechanism of the scratch test is shearing (plastic flow). The profile of scratch cross section for UFG cpTi after AO (formed nanotubes on UFG cpTi surface) shows that PA is significantly higher than GA which indicates that the dominant mechanism for removing materials and forming materials fragments during the scratch test is ploughing, Fig. 6b. Also, the profile of scratch cross section for UFG cpTi after AO shows that groove (scratch) depth is 63 nm, while groove (scratch) width is about 4 μm, Fig. 6b. The profile of scratch cross section for UFG cpTi shows that groove (scratch) depth is 212 nm, while groove (scratch) width is about 35 μm, while PA is slightly less than GA, indicating that dominant mechanism for removing materials and forming materials fragments during scratch test could be rubbing or shearing, Fig. 6a. In most cases, the scratch width controls the wear, while the depth or volume loss is more important for the wear resistance application, /44/. Values of scratch width and scratch depth depend on scratch test conditions, i.e., the applied force, shape and radius of the indenter tip /45, 46/. From Fig. 6, it is noted that the scratch depth and width for UFG cpTi surface are an order of magnitude higher than for UFG cpTi surface with nanotubes, with the same test conditions. Figure 7 presents the scratch test curve for UFG cpTi surface before and after AO. The slope of the scratch curve decreases with increasing displacement into surface (when the length of the nanotubes layer increases). The scratch curve slope is relatively stiff (along scratch distance) indicating a small possibility to annul the applied load. These facts could indicate that nanotube layer failure occurs along the length of the scratch.

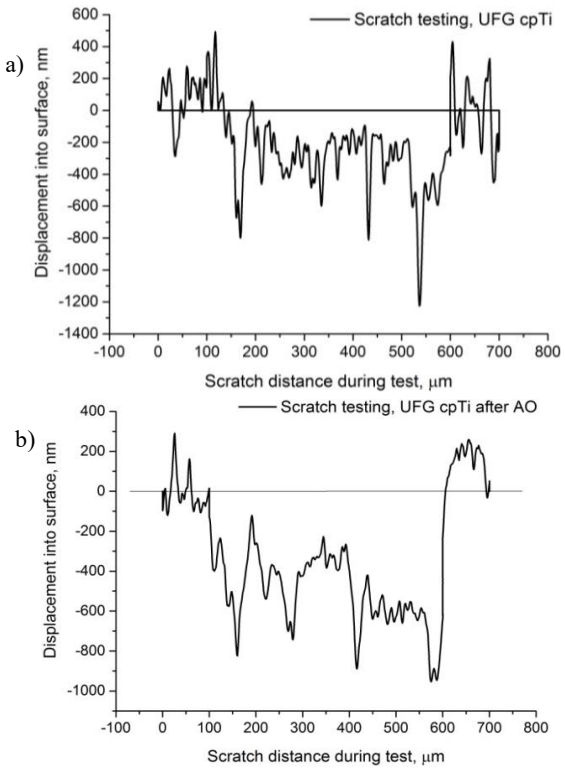

Figure 7. Scratch test curve of UFG cpTi surface: a) before; and b) after AO.

Scratch test curves show three regions, the ductile, transition (brittle-ductile) and brittle region, while large fluctuations occur at the beginning of region change. According to literature /45/, the appearance and changes in the diagram, as well as the characteristics of scratch surface morphology, depend on normal loading rate, indenter and its direction, but this indicates that the above-mentioned three regions constitute each scratch test curve. Figure 8 shows morphological characteristics of scratch and surface damage after the scratch test for UFG cpTi after AO at: a) lower, and b) higher mag-

nification. As can be seen, the scratch exists with visible lateral accumulation of material on both sides of the scratch edge.

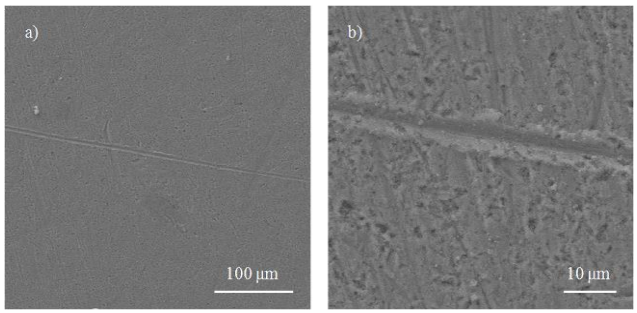

Figure 8. Scratched nanostructure oxide layer formed on UFG cpTi after AO for 60 min. at: a) lower; and b) higher magnifications.

After AO of UFG cpTi, the scratch track becomes wider, rougher, and less uniform, with more pronounced edges, Fig. 8b. The surrounding area exhibits fractured or fragmented debris, reflecting the removal or crushing of the nanotubular oxide layer. Scratch borders contain irregular ridge-like accumulations, suggesting that the brittle nanotube layer tends to fracture and spall instead of deforming plastically. Fine cracks and microcavities appear along the scratch path, corresponding to the collapse of nanotubes under mechanical load. The anodised surface of UFG cpTi, composed of TiO_2 nanotubes, displays brittle behaviour. The nanotube layer cannot sustain high shear stresses; instead, it fractures, producing a rough discontinuous scratch morphology. The deeper penetration of the indenter through the porous oxide also contributes to increased roughness of the scratch.

Corrosion resistance of UFG cpTi in Ringer's solution, after AO for 60 min.

- Potentiodynamic method

Figure 9 shows polarisation curves for UFG cpTi before and after AO during 60 min. in Ringer's solution pH = 5.5, while estimates of corrosion potential, E_{corr}, and corrosion current density, j_{corr}, are given in Table 6. Low corrosion current density values of the order of magnitude greater than 10^{-7} Acm^{-2} for tested materials, indicate exceptional stability against corrosion in simulated human body conditions. From the curves shown in Fig. 9 and the results in Table 6, the corrosion current density values are lower for UFG cpTi after AO, compared to UFG cpTi before AO in Ringer's solution. Ultrafine-grained commercially pure Ti (purity grade 2) after AO for 60 min. shows $j_{corr} = 33.7 \cdot 10^{-9}$ Acm^{-2} which is significantly lower than the corrosion current density for UFG cpTi before AO ($127 \cdot 10^{-9}$ Acm^{-2}).

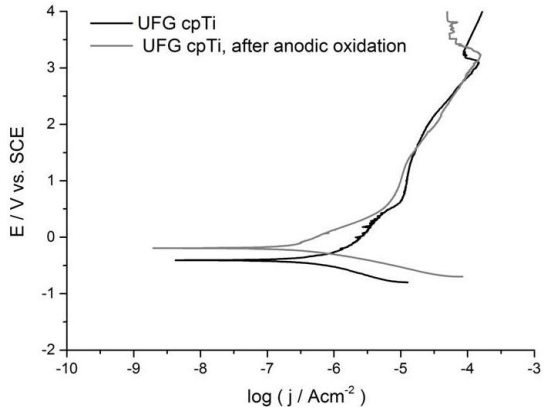

Figure 9. Potentiodynamic polarisation curves of UFG cpTi before and after AO.

Table 6. Electrochemical parameters of UFG cpTi before and after AO.

Material	UFG cpTi	UFG cpTi, after AO 60 min.
E_{corr} (V)	-0.41	-0.18
j_{corr} (nAcm^{-2})	127	33.7

By comparing the electrochemical parameters obtained for UFG cpTi before and after AO in artificial saliva solution and Ringer's solution, it can be concluded that the corrosion resistance of both surface-modified and unmodified material is lower in Ringer's solution, /40/. Namely, UFG cpTi after AO shows a $j_{corr} = 31.6 \cdot 10^{-9}$ Acm^{-2} in artificial saliva solution /41/, slightly lower than the corrosion current density for UFG cpTi ($33.7 \cdot 10^{-9}$ Acm^{-2}) after AO in Ringer's solution. However, UFG cpTi shows significantly better corrosion resistance in artificial saliva than in Ringer's solution. The reason for this behaviour of the material could be the chemical composition of the solution. Namely, Ringer's solution contains a larger amount of Cl^- ions compared to artificial saliva solution, and it is known from literature that the influence of these ions on the corrosion resistance of Ti-based materials is great, /46/. Based on the given equation, corrosion rate per year can be calculated using corrosion current density, j_{corr}, /47/:

$$\text{Corrosion rate (mm/yr)} = (0.00327 \cdot j_{corr} \cdot EW)/\rho \,. \quad (1)$$

Here, ρ is density of the material; and EW is the equivalent weight for the material.

The equivalent weight for Ti is about 16 under moderated acid conditions. The equation shows that corrosion rate increases with increasing corrosion current density. Using Eq.(1) it is obtained that corrosion rate value for UFG cpTi is 1.1 μm/year, while after AO and forming of self-regular nanotube oxide layer on the surface of UFG cpTi, the corrosion rate decreases to 0.29 μm/year. Figure 10 presents the comparison of corrosion rates of UFG cpTi and UFG cpTi after AO.

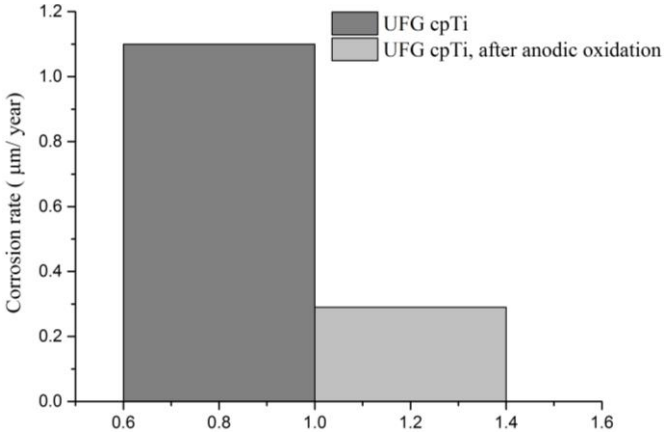

Figure 10. Corrosion rates of UFG cpTi and UFG cpTi after AO.

Bhola et al. /47/ report that commercially pure Ti has a lower corrosion rate than Ti-6Al-4V alloy, while both materials show corrosion a rate of 10^{-13} mm/yr for corrosion current density of 10^{-9} A/cm^2. Typically, corrosion rate for

Ti in the passive area is less than 0.02 mm/yr and maximum corrosion rate accepted for biomedical application is below 0.13 mm/yr, /48/. Lebea et al. /49/ show that 3D-printed Ti-6Al-4V has a higher corrosion rate (~ 2.8890 mm/year) in Ringer's solution, compared to the corrosion rate (~ 1.8938 mm/year) in NaCl body fluid. The authors explain this phenomenon by the ionic composition of Ringer's solution (K^+, Ca^{2+}, etc.) and possible porosity or additive microstructural effects. Kumrular et al. /50/ examine cpTi grades 1 and 5 (Ti-6Al-4V) in Ringer's solution with pH = 7 and pH = 3.5. The corrosion rate is 0.001-0.012 mm/year for pH = 7, and ~ 0.021 mm/year for pH = 3.5. Lower pH increases corrosion rate; damage seems more uniform, current densities correlate; a grouped comparison shows that Ti performs better than many stainless steel/gold wires. The lowest corrosion rates in Ringer's solution for Ti alloys under moderate conditions tend to be in the range from 10^{-4} to 10^{-3} mm/year, especially for alloys with a very passive surface (such as Ti-6Al-4V, or more highly alloyed/optimised types). Higher rates (of the order of ~ 10^0 mm/year, or multiple mm/year) appear in more aggressive or defective materials (e.g., 3D-printed with defects, porosity, or less stable passive film) under similar simulated body fluid conditions. This suggests that the manufacturing method, porosity, surface finish, and alloy composition strongly influence corrosion damage. The surface condition and passive film stability are key for better heat treatments, smoother surface finish, and alloying elements that stabilise the oxide or reduce defect formation improve the resistance (lower corrosion rates, lower current densities) in the case of Ti-6Al-4V alloy, /51/.

- Electrochemical impedance spectroscopy (EIS)

The electrochemical impedance spectrum is presented as a Nyquist (Fig. 11) and Bode (Fig. 12) diagram. All samples show characteristics of corrosion resistance.

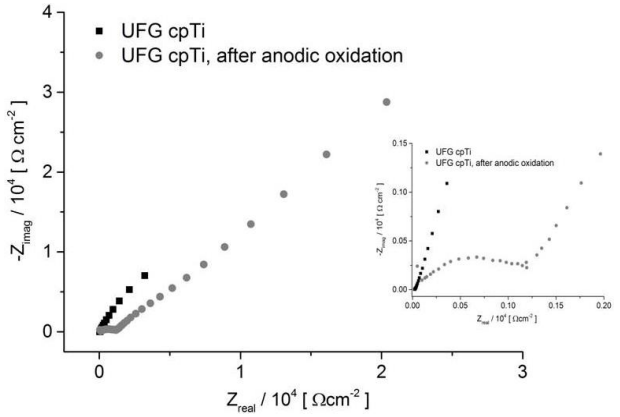

Figure 11. Nyquist plot of UFG cpTi before and after AO.

The obtained fitting results for the tested materials are given in Table 7. It can be observed that the corrosion resistance of the outer porous layer, R_p, is lower than that of the inner barrier layer, R_b, indicating that surface protection with the outer porous layer is worse than with the compact barrier layer.

The improvement in corrosion resistance of UFG cpTi after AO is clearly visible based on the results shown in Table 7. EIS analysis data, in the case of UFG cpTi after AO are successfully calculated using three series-connected equivalent circuits (EC). The resistance of the bottom of the nanotube, R_3 (R_{nb}), is greater than the resistance of the walls of the nanotube, R_2 (R_{nv}).

The results confirm the better stability of the barrier layer compared to the porous layer. The thickness of the oxide layer on the surface of UFG cpTi after AO, is greater than that of UFG cpTi before AO. It is also shown that the capacitance of the barrier layer, CPE_3, is less than the capacitance of the porous layer, CPE_2. As can be seen from the results in Table 7, the coefficient n has values ranging from 0.62 to 0.78. The results show that the formation of a nanotube oxide layer on the surface of UFG cpTi using AO increases the corrosion resistance compared to UFG cpTi before the AO.

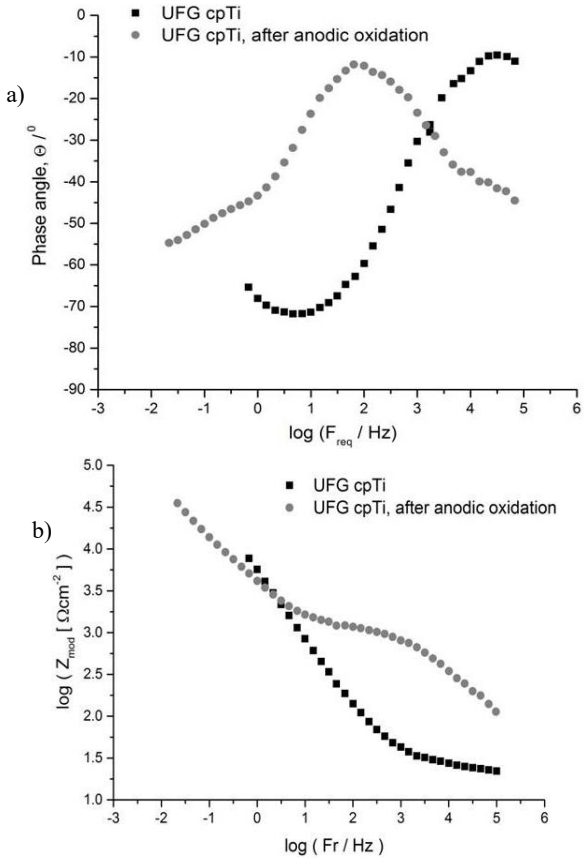

Figure 12. Graphic representation of Bode plots of: a) phase angles; and b) modulus of UFG cpTi before and after AO.

Table 7. Electrochemical impedance spectroscopy results of UFG cpTi before and after AO.

Material	Anod. time (min)	R_0 (Ω)	R_1 (Ωcm^2)	CPE_1		R_2 (Ωcm^2)	CPE_2		R_3 (Ωcm^2)	CPE_3	
				$Y_0 \cdot 10^7$ (Ω^{-1}cm^{-2})	n		$Y_0 \cdot 10^7$ (Ω^{-1}cm^{-2})	n		$Y_0 \cdot 10^7$ (Ω^{-1}cm^{-2})	n
UFG cpTi	/	30.69	$1.67 \cdot 10^2$	$1.81 \cdot 10^{-7}$	0.78	$4.31 \cdot 10^4$	$1.91 \cdot 10^{-7}$	0.89	/	/	/
	60	31.25	$1.18 \cdot 10^3$	$2.6 \cdot 10^{-6}$	0.62	$4.46 \cdot 10^4$	$8.21 \cdot 10^{-7}$	0.66	$1.14 \cdot 10^6$	$3.98 \cdot 10^{-7}$	0.75

CONCLUSION

Anodic oxidation can lead to the formation of nanotubes as a part of the oxide layer on the surface of UFG cpTi in the electrolyte of orthophosphoric acid with the presence of F-ions during 60 min. 60 minutes appear as optimal duration, producing a uniform, well-ordered nanotube array with consistent tube geometry. Shorter times (30 min) cannot produce fully developed tubes, while longer times (90-120 min) promote structural damage due to continuous chemical dissolution, resulting in wall thinning, tube collapse, and surface roughening. Morphological differences are critical because nanotube ordering, integrity, and uniformity influence corrosion resistance, osseointegration, and mechanical stability of the modified surface. Scratch test results show that AO drastically modifies the mechanical response of UFG cpTi during scratch loading. The scratch depth and width for untreated UFG surface are an order of magnitude higher than for the UFG cpTi surface with nanotubes. Results show that AO leads to an increase in corrosion resistance, a decrease of the corrosion rate of UFG cpTi in the Ringer solution with pH = 5.5. Corrosion resistance of UFG cpTi after AO is almost four times better than before AO.

ACKNOWLEDGEMENTS

This work is supported by the Ministry of Science, Technological Development and Innovation of the Republic of Serbia (Contracts No. 451-03-47/2025-01/200135 and 451-03-47/2025-01/200287). The authors acknowledge a very important role of the late Prof. Marko Rakin (1966-2023), who was the initiator of research activities in the field of Ti-based biomaterials at our University. The authors also acknowledge Dr. Anton Hohenwarter from the Department of Materials Science, Montanuniversität Leoben, Austria, for his help in the preparation of UFG samples.

REFERENCES

1. Barjaktarević, D., Dimić, I., Cvijović-Alalgić, I., et al. (2017), *Corrosion resistance of high pressure torsion obtained commercially pure titanium in acidic solution*, Tech. Gazette, 24(6): 1689-1695. doi: 10.17559/TV-20160303141534
2. Silva, R.C.S., Agrelli, A., Andrade, A.N., et al. (2022), *Titanium dental implants: An overview of applied nanobiotechnology to improve biocompatibility and prevent infections*, Mater. 15(9): 3150. doi: 10.3390/ma15093150
3. Browne, M., Gregson, P.J. (2001), *Effect of mechanical surface pretreatment on metal ion release*, Biomater. 21(4): 385-392. doi: 10.1016/s0142-9612(99)00200-8
4. Cvijović-Alagić, I., Rakin, M. (2008), *Integrity of biomedical implants of titanium alloys (first part)*, Struct. Integr. Life, 8(1): 31-40.
5. Ristić, Lj. (2006), *Dental alloys and corrosion*, Vojnosanitetski pregled, 63(12): 1033-1037. (in Serbian)
6. Cortada, M., Giner, L., Costa, S., et al. (2009), *Galvanic corrosion behavior of titanium implants coupled to dental alloys*, J Mater. Sci. Mater. Med. 11(5): 287-293. doi: 10.1023/a:1008905229522
7. Okazaki, Y., Gotoh, E. (2005), *Comparison of metal release from various metallic biomaterials in vitro*, Biomater. 26(1): 11-21. doi: 10.1016/j.biomaterials.2004.02.005
8. Joseph, L.A., Israel, O.K., Edet, E.J. (2009), *Comparative evaluation of metal ions release from titanium and Ti-6Al-7Nb into bio-fluids*, Dent. Res. J (Isfahan), 6(1): 7-11.
9. Nejatidanesh, F., Savabi, O., Yazdanparast, Y. (2005), *An investigation on metallic ion release from four dental casting alloys*, J Dent. Tehran Univ. Med. Sci. 2(4): 168-173.
10. Eliaz, N. (Ed.), Degradation of Implant Materials, 1st Ed., Springer, New York, 2012. doi: 10.1007/978-1-4614-3942-4
11. Blackwood, D.J., Chua, A.W.C., Seah, K.H.W., et al. (2000), *Corrosion behaviour of porous titanium-graphite composites designed for surgical implants*, Corr. Sci. 42(3): 481-503. doi: 10.1016/S0010-938X(99)00103-1
12. Eliaz, N. (2019), *Corrosion of metallic biomaterials: a review*, Mater. 12(3): 407-499. doi: 10.3390/ma12030407
13. Ossowska, A., Zieliński, A. (2020), *The mechanisms of degradation of titanium dental implants*, Coatings, 10(9): 836. doi: 10.3390/coatings10090836
14. Yu, T., Yin, H., Zhou, Y., et al. (2017), *Electrochemical preparation of porous Ti-13Zr-13Nb alloy and it's corrosion behavior in Ringer's solution*, Mater. Trans. 58(3): 326-330. doi: 10.2320/matertrans.MK201627
15. Robin, A., Carvalho, O.A.S. (2013), *Influence of pH and fluoride species on the corrosion behavior of Ti-xNb-13Zr alloys in Ringer's solution*, Adv. Mater. Sci. Eng. 2013(1): 434975. doi: 10.1155/2013/434975
16. Nunes, A.R.V., dos Reis Barros, C.D., Carvalho, G.G., et al. (2025), *Corrosion resistance of an alternative thermomechanically processed Ti-23.6Nb-5.1Mo-6.7Zr alloy for biomedical applications*, Metals, 15(9): 962. doi: 10.3390/met15090962
17. Valiev, R.Z., Estrin, Y., Horita, Z., et al. (2006), *Producing bulk ultrafine-grained materials by severe plastic deformation*, J Mater. Sci. 58: 33-39. doi: 10.1007/s11837-006-0213-7
18. Valiev, R.Z., Langdon, T.G. (2006), *Principles of equal-channel angular pressing as a processing tool for grain refinement*, Prog. Mater. Sci. 51(7): 881-981. doi: 10.1016/j.pmatsci.2006.02.003
19. Minagar, S., Berndt, C.C., Wanga, J., et al. (2012), *A review of the application of anodization for the fabrication of nanotubes on metal implant surfaces*, Acta Biomater. 8(8): 2875-2888. doi: 10.1016/j.actbio.2012.04.005
20. Sanusi, K., Makinde, O., Oliver, G. (2012), *Equal channel angular pressing technique for the formation of ultra-fine grained structures*, South Africa J Sci. 108(9/10): 1-7. doi: 10.4102/sajs.v108i9/10.212
21. Azushima, A., Kopp, R., Korhonen, A., et al. (2008), *Severe plastic deformation (SPD) processes for metals*, CIPR Annals, 57(2): 716-735. doi: 10.1016/j.cirp.2008.09.005
22. Yang, J., Song, Y., Dong, K., Han, E.-H. (2023), *Research progress on the corrosion behavior of titanium alloys*, Corr. Rev. 41(1): 5-20. doi: 10.1515/corrrev-2022-0031
23. Fattah-alhosseini, A., Imantalab, O., Ansari, G. (2017), *The role of grain refinement and film formation potential on the electrochemical behavior of commercial pure titanium in Hank's physiological solution*, Mater. Sci. Eng.: C. 71: 827-834. doi: 10.1016/j.msec.2016.10.072
24. Zhang, L., Han. Y. (2010), *Effect of nanostructured titanium on anodization growth of self-organized TiO_2 nanotubes*, Nanotechnology, 21(5): 055602. doi: 10.1088/0957-4484/21/5/055602
25. Miyamoto, H. (2016), *Corrosion of ultrafine grained materials by severe plastic deformation, an overview*, Mater. Trans. 57(5): 559-572. doi: 10.2320/matertrans.M2015452
26. Gu, Y., Jiang, J., Ma, A., et al. (2022), *Enhanced corrosion behavior of ultrafine-grained pure titanium in simulated high-temperature seawater*, J Mater. Res. Technol. 19: 1-6. doi: 10.1016/j.jmrt.2022.05.032

27. Yu, Z., Dong, Y., Li, X., et al. (2020), *Study on corrosion behavior of ultrafine-grained Ti-6Al-7Nb fabricated by equal channel angular pressing*, Metals, 10(7): 950. doi: 10.3390/met10070950
28. Oliveira, N.T.C., Ferreira, E.A., Duarte, L.T., et al. (2006), *Corrosion resistance of anodic oxides on the Ti-50Zr and Ti-13Nb-13Zr alloys*, Electrochimica Acta, 51(10): 2068-2075. doi: 10.1016/j.electacta.2005.07.015
29. Saji, V.S., Choe, H.C., Brantley, W.A. (2009), *An electrochemical study on self-ordered nanoporous and nanotubular oxide on Ti-35Nb-5Ta-7Zr alloy for biomedical applications*, Acta Biomaterialia, 5(6): 2303-2310. doi: 10.1016/j.actbio.2009.02.017
30. Mihajlović, D.R., Medjo, B.I., Bajat, J.B., Djokić, V.R. (2025), *High-pressure torsion and anodic oxidation as a method for surface engineering of Ti-13Nb-13Zr biomedical alloy*, Metals, 15(9): 997. doi: 10.3390/met15090997
31. Mello, M.G., Taipina, M.O., Rabelo, G., et al. (2017), *Production and characterization of TiO_2 nanotubes on Ti-Nb-Mo-Sn system for biomedical applications*, Surf. Coat. Technol. 326 (Part A): 126-133. doi: 10.1016/j.surfcoat.2017.07.027
32. Hu, N., Gao, N., Starink, M.J. (2016), *The influence of surface roughness and high-pressure torsion on the growth of anodic titania nanotubes on pure titanium*, Appl. Surf. Sci. 387: 1010-1020. doi: 10.1016/j.apsusc.2016.07.036
33. Macák, J.M., Tsuchiya, H., Schmuki, P. (2005), *High-aspect-ratio TiO_2 nanotubes by anodization of titanium*, Angew. Chem. Int. Ed. Engl. 44(14): 2100-2102. doi: 10.1002/anie.200462459
34. Regonini, D., Bowen, C.R., Jaroenworaluck, A., Stevens, R. (2013), *A review of growth mechanism, structure and crystallinity of anodized TiO_2 nanotubes*, Mater. Sci. Eng.: R: Rep. 74 (12): 377-406. doi: 10.1016/j.mser.2013.10.001
35. Roy, P., Berger, S., Schmuki, P. (2011), *TiO_2 nanotubes: synthesis and applications*, Angew. Chem. Int. Ed. Engl. 50(13): 2904-2939. doi: 10.1002/anie.201001374
36. Valiev, R.Z., Zhilyaev, A.P., Langdon, T.G., Bulk Nanostructured Materials: Fundamentals and Applications, Wiley, 2014. doi: 10.1002/9781118742679
37. Poinern, G.E.J., Ali, N., Fawcett, D. (2011), *Progress in nano-engineered anodic aluminum oxide membrane development*, Materials 4(3): 487-526. doi: 10.3390/ma4030487
38. Barjaktarević, D.R., Djokić, V.R., Bajat, J.B., et al. (2019), *The influence of the surface nanostructured modification on the corrosion resistance of the ultrafine-grained Ti-13Nb-13Zr alloy in artificial saliva*, Theor. Appl. Fract. Mech. 103: 102307. doi: 10.1016/j.tafmec.2019.102307
39. Barjaktarević, D., Medjo, B., Štefane, P., et al. (2021), *Tensile and corrosion properties of anodized ultrafine-grained Ti-13Nb-13Zr biomedical alloy obtained by high-pressure torsion*, Met. Mater. Int. 27: 3325-3341. doi: 10.1007/s12540-020-00837-z
40. Mihajlović, D., Rakin, M.P., Bajat, J.B., Đokić, V.R. (2023), *Corrosion stability of the anodized ultrafine-grained titanium in the human body solution*, Metall. Mater. Data, 1(1): 7-11. doi: 10.30544/MMD3
41. Barjaktarević, D.R., Rakin, M.P., Djokić, V.R. (2018), *Characterisation of the nanotubular oxide layer formed on the ultrafine-grained titanium*, Metall. Mater. Eng. 24(4): 261-270. doi: 10.30544/402
42. Gittens, R.A., Scheideler, L., Rupp, F., et al. (2014), *A review on the wettability of dental implant surfaces II: Biological and clinical aspects*, Acta Biomater. 10(7): 2907-2918. doi: 10.1016/j.actbio.2014.03.032
43. Pratap, A., Divse, V., Goel, S., Joshi, S.S. (2022), *Understanding the surface generation mechanism during micro-scratching Ti-6Al-4V*, J Manuf. Proc. 82: 543-558. doi: 10.1016/j.jmapro.2022.08.014
44. Rajendhran, N., De Baets, P., Huang, S., et al. (2021), *Single-point scratch testing for understanding particle engagement in abrasion of multiphase materials*, Wear, 476: 203689. doi: 10.1016/j.wear.2021.203689
45. Tang, K., Ou, W., Mao, C., et al. (2023), *Material removal characteristics of single-crystal 4H-SiC based on varied-load nanoscratch tests*, Chin. J Mech. Eng. 36: 111. doi: 10.1186/s10033-023-00944-z
46. Prando, D., Brenna, A., Diamanti, M.V., et al. (2017), *Corrosion of titanium: Part 1: Aggressive environments and main forms of degradation*, J Appl. Biomater. Funct. Mater. 15: 291-302. doi: 10.5301/jabfm.5000387
47. Bhola, R., Bhola, S.M., Mishra, B., Olson, D.L. (2009), *Electrochemical behavior of titanium and its alloys as dental implants in normal saline*, Adv. Phys. Chem. 2009(1): 574359. doi: 10.1155/2009/574359
48. Bhola, R., Bhola, S.M., Mishra, B., Olson, D.L. (2011), *Corrosion in titanium dental implants/prostheses - A review*, Trends Biomater. Artif. Organs, 25(1): 34-46.
49. Lebea, L., Ngwangwa, H.M., Desai, D.A., Nemavhola, F. (2022), *Corrosion resistance of 3D-printed titanium alloy Ti64-ELI parts for dental application*, Appl. Bionics Biomech. 2022 (1): 1804417. doi: 10.1155/2022/1804417
50. Kumrular. B., Cicek. O., Dağ, İ.E., et al. (2023), *Evaluation of the corrosion resistance of different types of orthodontic fixed retention appliances: A preliminary laboratory study*, J Funct. Biomater. 14(2): 81. doi: 10.3390/jfb14020081
51. Luqman, M., Seikh, A.H., Sarkar, A., et al. (2020), *A comparative study of the electrochemical behavior of α and β phase Ti6Al4V alloy in Ringer's solution*, Crystals, 10(3): 190. doi: 10.3 390/cryst10030190